

The final version of this article can be accessed at:
Nature Materials 12, 1045-1049 (2013)
<http://www.nature.com/doifinder/10.1038/nmat3710>

Title: Direct Measurement of Molecular Motion in Organic Semiconductors

Authors: Alexander S. Eggeman,^{1*} Steffen Illig,^{2*} Alessandro Troisi,³
Henning Sirringhaus² and Paul A. Midgley¹

Affiliations: ¹Department of Materials Science and Metallurgy, University of Cambridge,
Pembroke Street, Cambridge CB2 3QZ, UK

²Cavendish Laboratory, University of Cambridge, JJ Thompson Avenue, Cambridge,
CB3 0HE, UK

³Department of Chemistry and Centre for Scientific Computing, University of Warwick,
Gibbet Hill Road, Coventry, CV4 7AL, UK

*To whom correspondence should be addressed; E-mail: ase25@cam.ac.uk
and si278@cam.ac.uk

Abstract: Many of the remarkable electrical and optical properties of organic semiconductors are governed by the interaction of electronic excitations with intra- and intermolecular vibrational modes. However, in specific systems this interaction is not understood in detail at a molecular level and this has been due, at least in part, to the lack of easy-to-use and widely available experimental probes of the structural dynamics. Here we demonstrate that electron diffraction on crystalline thin films of molecular semiconductors, such as 6,13-bistriisopropyl-silylethynyl (TIPS) pentacene, is a powerful tool to probe directly correlated intermolecular motions and lattice phonons. The amplitude and direction of the dominant molecular motions can be determined by

comparison of the diffuse scattering with simulations and molecular dynamics calculations. This technique could enable a much deeper understanding of the structural dynamics in a wide range of organic semiconductors.

One Sentence Summary: Direct measurement of lattice vibrations in an organic semiconductor is reported and used to explain the transport behaviour of TIPS-pentacene.

Main Text: In van-der-Waals bonded molecular solids electronic excitations couple strongly to intra- and intermolecular molecular vibrations leading to large reorganisation energies and polaron formation and giving rise to many of the unique electrical and optical properties of these materials (1). In particular, in molecular crystals the coupling of electronic excitations, such as charge carriers or excitons, to low-energy thermal lattice fluctuations such as soft librational or translational phonon modes is believed to be responsible for the observed decrease in carrier mobility with increasing temperature (2). Thermal lattice fluctuations lead to temporal variations of the transfer integrals, as these are highly sensitive to the relative intermolecular positions of adjacent molecules. This dynamic disorder has been predicted theoretically to result in localisation of the charge carriers (3). Recently, it has been reported that this dynamic disorder model provides a consistent framework for understanding the electrical and optical properties of charge carriers in crystalline, high mobility molecular semiconductors, such as TIPS-pentacene, and is able to explain variations in charge carrier mobility with molecular structure and crystal packing (4). A detailed understanding of the nature and strength of thermal lattice fluctuations as a function of molecular structure and intermolecular packing is urgently needed to guide the design of novel molecules with even higher charge carrier mobilities.

Unfortunately, experimental studies of the coupling between electronic excitations and molecular structure are rarely based on direct measurements of the structural dynamics, but on inferring molecular motions from molecular dynamics (MD) simulations (3) or from indirect measurements (5). This is because of a lack of experimental techniques that are able to probe

directly the structural dynamics in these materials. In principle, X-ray scattering provides a powerful method to experimentally investigate thermal motion in molecular crystals (6). However, the displacements are relatively small, typically less than 1 Å, and thus synchrotron measurements would be needed to provide the required energies. Furthermore, X-ray scattering requires typically large single-crystalline areas to avoid averaging over several crystalline domains within the area exposed to the X-ray beam.

In this paper we present a comparatively simple and widely applicable electron diffraction method to determine quantitatively intermolecular motions in molecular crystals. We apply this technique to study the lattice dynamics of thin films of TIPS-pentacene (shown schematically in Figure 1A), a widely researched, high mobility organic semiconductors for applications in flexible electronics (7).

Electron diffraction in the transmission electron microscope (TEM) is especially well-suited to analysing organic crystals because of three factors. (i) Electrons interact far more strongly with matter than X-rays enabling weak diffuse scattering to be detected more readily; (ii) information can be gathered out to high scattering angles, equivalent to $<0.5\text{\AA}$ resolution even for light atoms (8) and (iii) single crystal patterns can be acquired with sub-nanometre spatial resolution, from polycrystalline regions and thin films, avoiding the need for the large samples required for similar X-ray and neutron diffraction experiments. However, care is needed to avoid beam damage and to account for dynamical effects; we comment further on both later in this article.

Uniform TIPS-pentacene films (with typical grain sizes of several hundred microns) were produced using a novel combination of drop-cast and flotation procedures that is applicable to most non water-soluble organic semiconductors (Supporting Information). The crystal structure of TIPS-pentacene is known to be triclinic (space group $P\bar{1}$) with cell parameters $a=7.565\text{\AA}$, $b=7.750\text{\AA}$, $c=16.835\text{\AA}$, $\alpha=89.15^\circ$, $\beta=78.42^\circ$ and $\gamma=83.63^\circ$ (9). The crystal structure as viewed

parallel to the [001] direction is shown in Figure 1B. Small -angle convergent-beam electron diffraction (CBED) patterns, were acquired from TIPS-pentacene film, an example is shown in Figure 1C (in this case the sample was cooled to 100 K to improve the clarity of the pattern and the longevity of the films under irradiation). This [001] pattern shows streaks of diffuse intensity (almost) parallel to [120]* (the [120]* direction can be seen from the streak passing through $4\bar{5}0$ and $5\bar{3}0$) reflections indicating structural disorder. Patterns from other zone axes (Supplementary Information) show similar diffuse streaks, consistent with these being traces of a single set of planes of diffuse scattering whose normal is parallel (within experimental error) to $[2\bar{1}0]^*$.¹

Planes of diffuse scattering indicate a 1-D breakdown of structural correlation, as would be the case for thermally driven linear motion and so by analysis of the form and intensity of the diffuse scattering it is possible to identify the atomic displacements associated with the disorder (*10*). Figure 1D shows schematically how a well-defined linear motion in real space creates a range of interplanar angles (δ, ϵ, θ) and planar spacings (l, m, n). This results in the corresponding reciprocal lattice points lying on a well-defined line (Figure 1E). The displacement vector of the atoms in the structure is perpendicular to this line and thus the normal to the plane of diffuse scattering defines the direction of any displacement. The molecular and crystal structure of TIPS-pentacene suggests a possible source of atomic displacement through a longitudinal motion of the pentacene fragment (which lies normal to the streak direction in Figures 1B and C). The enmeshed isopropylsilyl side-chains together with the cofacial $\pi - \pi$ stacking creates a linear channel in which the pentacene fragment resides; the side-chains should provide sufficient flexibility to allow some deviation in the position of each pentacene fragment in the structure. The pentacene fragment long axis lies, to a very good approximation, parallel to $[2\bar{1}0]$ (See Supporting Information) and thus the diffuse streaks seen (traces of the plane of diffuse

¹In fact the angle between $[120]^*$ and $[2\bar{1}0]^*$ is 88.24°

scattering) are consistent with a linear displacement along the pentacene long axis. The modulation of the intensity along the streaks is caused by the convolution with the shape transform of the pentacene molecule.²

To validate our method it was essential to ensure that (i) such displacements do not arise from beam-induced defects and that (ii) motions induced by the electron beam are minor. To show the latter, time series were recorded at 100 K and 300 K, each comprising 35 diffraction patterns. Figure 2A shows a selected area diffraction (SAD) pattern, from one of the time series recorded at 300 K. Linescans through the diffuse streaks (corrected for the Bragg reflections) yield intensity profiles and the evolution of such a profile is displayed by the blue lines in Figure 2b, which indicate an initial increase in streak intensity. Even at significantly higher electron doses (in this series 8.8×10^{-3} C/cm² was applied between images) than used for the actual data acquisition the increase never exceeded 30% of the initial value, showing that electron-beam induced motions are a source of error which tends to overestimate the actual molecular motion (Supplementary Information).

To investigate the former point above, electron diffraction patterns were recorded at ~ 10 K, using a liquid helium stage to reduce thermal effects. These showed a significant reduction in diffuse intensity, with the remaining energy at 10 K (including the residual zero-point vibration) responsible for the non-zero intensity of the streaks (Supporting Information). This indicates that the displacements arise from dynamic motions within the structure rather than from static displacements such as defects; a result which was further strengthened by a closer examination of the time series. Figure 2B shows the evolution of the features indicated in the diffraction pattern (Fig. 2A), with the initial intensity of every feature normalised. The ± 120 reflections (green) and the diffuse streaks (blue) are associated strongly with the arrangement of the pentacene fragments and these remain mostly stable with applied electron dose. Other low order

²Just as the diffracted intensities are given by a convolution with the lattice basis

reflections (red) associated primarily with the side-chains are rapidly affected by the electron beam. This observation agrees well with other research (*11*) that indicated a four times higher beam sensitivity of TIPS-pentacene compared to unsubstituted pentacene, which can be explained by the different aromaticity of the molecule constituents. The delocalized π -electrons present on the pentacene fragment can ‘repair’ most ionization damage caused by the beam (much like graphite has been found to be immune to radiolysis (*12*)). By contrast the ionization of a bonding electron in one of the isopropylsilyl groups results in the breaking of its chemical bond.

Importantly, the absence of the effects of radiolysis suggests that knock-on damage is the primary degradation mechanism of the pentacene fragment and there is no reason that knock-on displacements should be correlated in a single direction that lies almost perpendicular to the electron beam. Since the presence of diffuse streaks however can be explained only by such structural correlation, static disorder has been excluded from consideration.

A ‘frozen-phonon’ model (*13*) of the structure was used to simulate the dynamical electron diffraction pattern (via a multislice calculation (*14*)) incorporating the pentacene phonon mode. The structure model comprised a static matrix of isopropylsilyl side-chains with a molecular substitution of the pentacene fragments. The fragment positions were displaced by a Gaussian standard deviation (σ) applied along the pentacene long-axis direction; allowing the amplitude of the phonon mode to be determined by refinement. For such a calculation a large supercell of TIPS-pentacene was required, which resulted in a fine sampling of reciprocal space and improved fidelity of the diffuse scattering simulation (*15*). The large supercell also enabled a statistically significant number of independent atomic displacements to be included in the calculation using graphical processing units (GPUs) (*16–18*). The calculation steps were optimised and made the calculation time for an 18×18 supercell sufficiently fast (1.07 s per slice, including preparing the potential map) to achieve reliable statistics by averaging each pattern over 50

runs.

A simulated diffraction pattern with $\sigma=0.07$ Å and crystal thickness of 55 nm (the sample thickness was determined by matching the dynamical Bragg intensities) is shown in Figure 3A; the arrangement of diffuse streaks appears very similar to the experiment, notably the modulated streaks at the correct distance from the centre of the pattern and the absence of a streak passing through the unscattered beam and the $h2h0$ reflections. The simulation used a parallel incident electron beam resulting in the Bragg reflections being δ -functions and so appearing almost uniformly intense compared to the weaker diffuse streaks. A quantitative comparison between the simulated and experimental patterns was achieved by matching linescans through the diffuse streaks; an example (labelled PQ in Figure 3A) is shown inset. By considering linescans across the entire pattern recorded at 100 K, a residual (R -factor (19)) calculation indicated that the best agreement occurred for $\sigma=0.07 \pm 0.02$ Å; the distribution of relative intermolecular distances (between centres of mass) arising from this phonon model was fit to a Gaussian with $\sigma_r=0.08 \pm 0.02$ Å. For experimental data recorded at room temperature, the minimum residual was found to be at $\sigma=0.09 \pm 0.02$ Å and a distribution of intermolecular distances with $\sigma_r=0.13 \pm 0.02$ Å.

Further validation of the phonon model was achieved by comparison with molecular dynamics (MD) calculations at 100 and 300 K following the method given in Troisi *et al.* (20). The atomic coordinates from the MD trajectory were used in two ways: to produce diffraction patterns for comparison with the previous experimental and simulated patterns and to quantify the longitudinal motion of the pentacene fragment. The trajectories provided atomic coordinates that were input into the same electron scattering calculation as used previously and the resulting simulated electron diffraction pattern is shown in Figure 3B. The general form of Bragg reflections and diffuse streaks is in good agreement with both the experimental and simulated diffraction patterns (Figures 1C and 3A); this supports both the phonon model chosen previously and the output trajectories of the MD simulations. However the supercell thickness used

for the MD simulation was fixed at 5.051 nm (to limit the size of the MD calculation), much thinner than the experimental crystal thickness making direct quantitative comparison difficult. Nevertheless, information about the specific phonon mode under scrutiny can be extracted from the MD trajectories. The intermolecular displacement of the pentacene fragment centres-of-mass was determined for temperatures between 30 and 300 K from MD simulations, the fitted σ_r for these distributions are shown in Figure 3C, along with the two experimental values. There is a good agreement at 300 K where the MD returns $\sigma_r = 0.127 \text{ \AA}$, which compares well with the 0.13 \AA refined from the scattering model. Likewise at 100 K, MD simulation returns $\sigma_r = 0.072 \text{ \AA}$ (c.f. 0.08 \AA for the scattering simulations).

There is little doubt that such large vibrational modes have the capability to significantly influence charge transfer in organic semiconductors, due to their narrow band structure and the high sensitivity of the transfer integral to intermolecular displacements (3, 21). Quantum chemical calculations in (20) provided a quantitative evaluation of the extent to which the electronic coupling between HOMOs localized on adjacent molecules changes as a function of the relative molecular displacement along the $[2\bar{1}0]$ direction of a TIPS-pentacene crystal. In Figure 3D this change (*top*) is compared with the distribution of relative displacements computed from the MD simulation (*bottom*), which is very similar to that inferred from the diffraction patterns. The observed displacements (of the order of tens of picometres) are sufficient to cause fluctuations of the intermolecular coupling of the same order of magnitude of its average value. This results in an expanded tail of trap states in the valence band of organic semiconductors which manifests itself in smaller localization lengths for higher temperatures. The negative μ -T dependence at higher temperatures that was observed in several high-performance organic semiconductors (22) and the evidence of charge carrier localization from charge modulation spectroscopy (4) can be both understood in terms of large fluctuations of the intermolecular distances that can be now probed directly and experimentally with the technique presented here.

We have shown that the streaks observed in the experimental diffraction pattern are generated by changes in the relative distance between close molecules. The simulation of the experimental pattern based on rigid molecular displacements and classical MD simulations (all modes included) are similar because the diffraction pattern is less affected by intramolecular motions and long wavelength acoustic modes that are included in the MD simulation but not in the rigid molecule model. Importantly, it is the relative displacement between molecules that has the largest influence on the electronic structure of molecular semiconductors, i.e. the analysis of the experimental diffraction pattern has the ability to provide information on the nuclear modes that matter most for charge transport. We have been able to observe similar diffuse scattering contrast in a broad range of molecular semiconductors as well as inorganic materials (Supporting Information) and this suggests that our technique is indeed widely applicable and provides a powerful tool to study the interplay between lattice dynamics and the transport of charges as well as excitons in functional materials with fine-scale microstructure.

References and Notes

1. V. Coropceanu, *et al.*, *Chemical Reviews* **107**, 926 (2007).
2. E. A. Silinsh, V. Capek, *Organic Molecular Crystals. Interaction, Localisation and Transport Phenomena* (AIP Press, New York, 1994).
3. A. Troisi, G. Orlandi, *The Journal of Physical Chemistry A* **110**, 4065 (2006).
4. J.-F. Chang, *et al.*, *Phys. Rev. Lett.* **107**, 066601 (2011).
5. W. C. Germs, K. Guo, R. A. J. Janssen, M. Kemerink, *Phys. Rev. Lett.* **109**, 016601 (2012).
6. F. Dénoyer, R. Comès, M. Lambert, A. Guinier, *Acta Crystallographica Section A* **30**, 423 (1974).

7. G. Gelinck, P. Heremans, K. Nomoto, T. D. Anthopoulos, *Advanced Materials* **22**, 3778 (2010).
8. D. A. Muller, B. Edwards, E. J. Kirkland, J. Silcox, *Ultramicroscopy* **86**, 371 (2001).
9. J. E. Anthony, J. S. Brooks, D. L. Eaton, S. R. Parkin, *Journal of the American Chemical Society* **123**, 9482 (2001).
10. R. L. Withers, *Z. Kristallogr.* **220**, 1027 (2005).
11. D. C. M. Jihua Chen, J. E. Anthony, *Journal of Materials Research* pp. 1701 – 1709 (2007).
12. F. Banhart, *Reports on Progress in Physics* **62**, 1181 (1999).
13. R. F. Loane, P. Xu, J. Silcox, *Acta Crystallographica Section A* **47**, 267 (1991).
14. E. J. Kirkland, *Advanced Computing in Electron Microscopy* (Plenum, 1998).
15. T. Proffen, R. B. Neder, *Diffuse scattering and defect structure simulations* (Oxford University Press, 2008).
16. E. Lindholm, J. Nickolls, S. Oberman, J. Montrym, *IEEE Micro* **28**, 39 (2008).
17. J. Tickner, *Computer Physics Communications* **181**, 1821 (2010).
18. C. Dwyer, *Ultramicroscopy* **110**, 195 (2010).
19. C. Giacovazzo, *et al.*, *Fundamentals of Crystallography* (Oxford University Press, 2002).
20. A. Troisi, G. Orlandi, J. E. Anthony, *Chemistry of Materials* **17**, 5024 (2005).
21. H. Siringhaus, T. Sakanoue, J.-F. Chang, *physica status solidi (b)* **249**, 1655 (2012).

22. N. A. Minder, S. Ono, Z. Chen, A. Facchetti, A. F. Morpurgo, *Advanced Materials* **24**, 503 (2012).
23. C. D. Dimitrakopoulos, D. J. Mascaró, *IBM Journal of Research and Development* **45**, 11 (2001).
24. M. J. Kim, H. W. Heo, Y. K. Suh, C. K. Song, *Organic Electronics* **12**, 1170 (2011).
25. J. Zuo, M. McCartney, J. Spence, *Ultramicroscopy* **66**, 35 (1996).
26. A. J. C. Wilson, *Nature* **150**, 151 (2006).
27. M. Abramoff, P. Magalhaes, S. Ram, *Biophotonics International* **11**, 36 (2004).
28. R. Vincent, D. M. Bird, J. W. Steeds, *Philosophical Magazine A* **50**, 765 (1984).

Acknowledgements Two of the authors, AE and PM, acknowledge financial support through EPSRC grant EP/H017712 and from the European Research Council under the European Union's Seventh Framework Programme (FP7/2007-2013)/ERC grant agreement 291522-3DIMAGE and the Seventh Framework Programme of the European Commission: ESTEEM2, contract number 312483, HS acknowledges the EPSRC for financial support through EP/G060738/1 and AT acknowledges the Leverhulme trust for support.

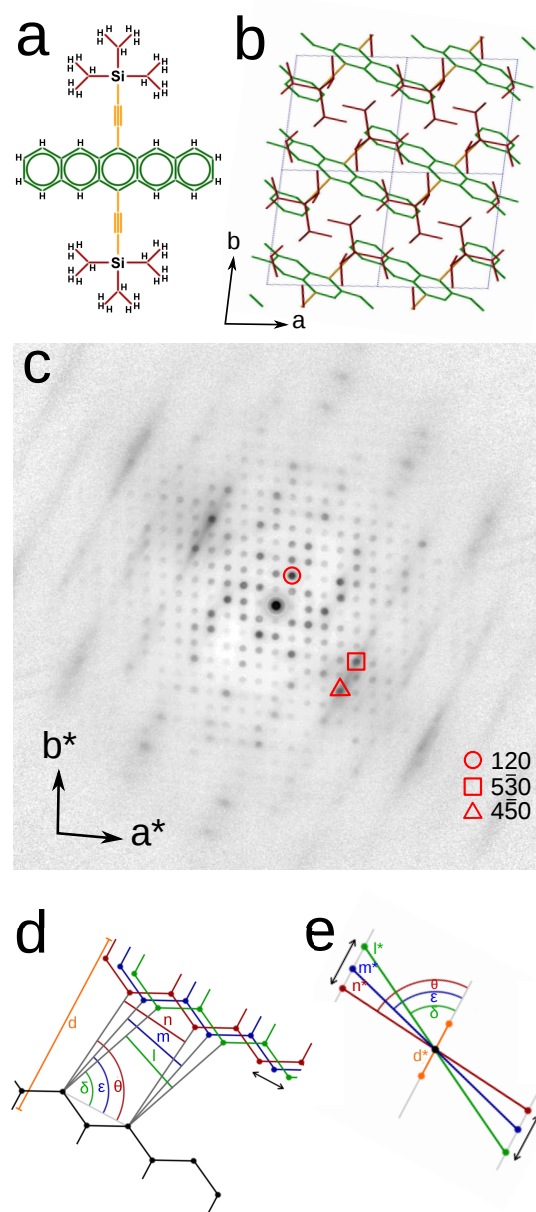


Figure 1: A) Schematic structure of the TIPS-pentacene molecule showing the conjugated π -electron density on the pentacene fragment. B) Ideal structure of the TIPS-pentacene crystal projected along [001]. C) Experimental electron diffraction pattern recorded from a TIPS-pentacene crystal parallel to [001], this has been adjusted to increase the visibility of the streaks at high scattering angles. D) The relationship between a linear motion in real-space and E) the diffuse scattering resultant in reciprocal space. Note the pentacene fragment in B) and C) are aligned parallel, resulting in the streak direction in D) and E) being parallel too.

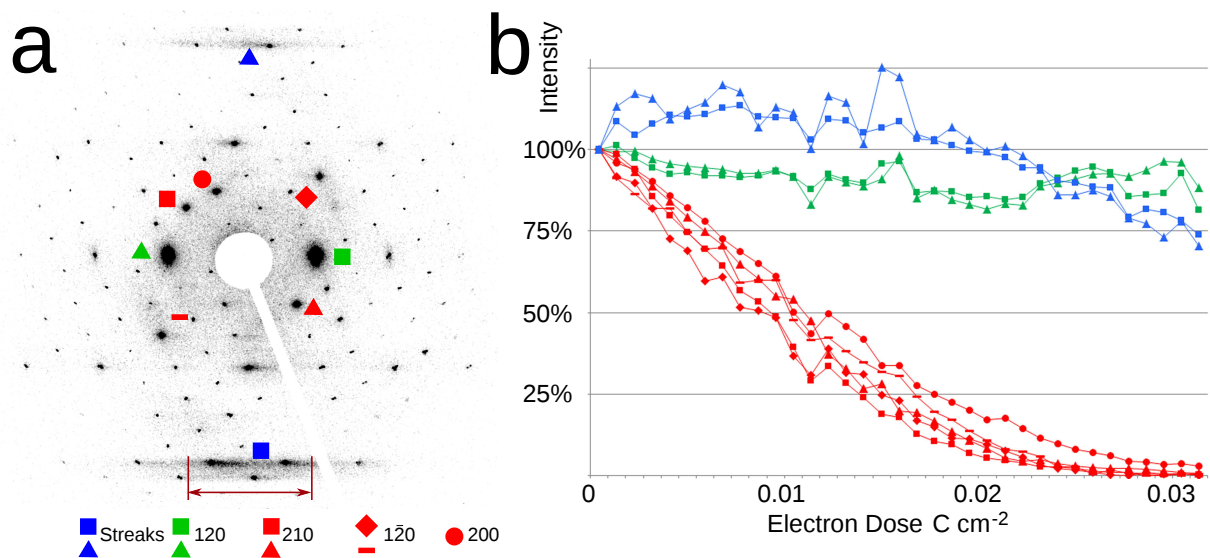


Figure 2: A) Uncorrected SAD pattern of TIPS-pentacene belonging to a time series of 35 exposures taken at 300 K. B) Intensity profiles with increasing electron dose of the streak (blue), ± 120 reflections (green) and other low order reflections (red) as indicated in A).

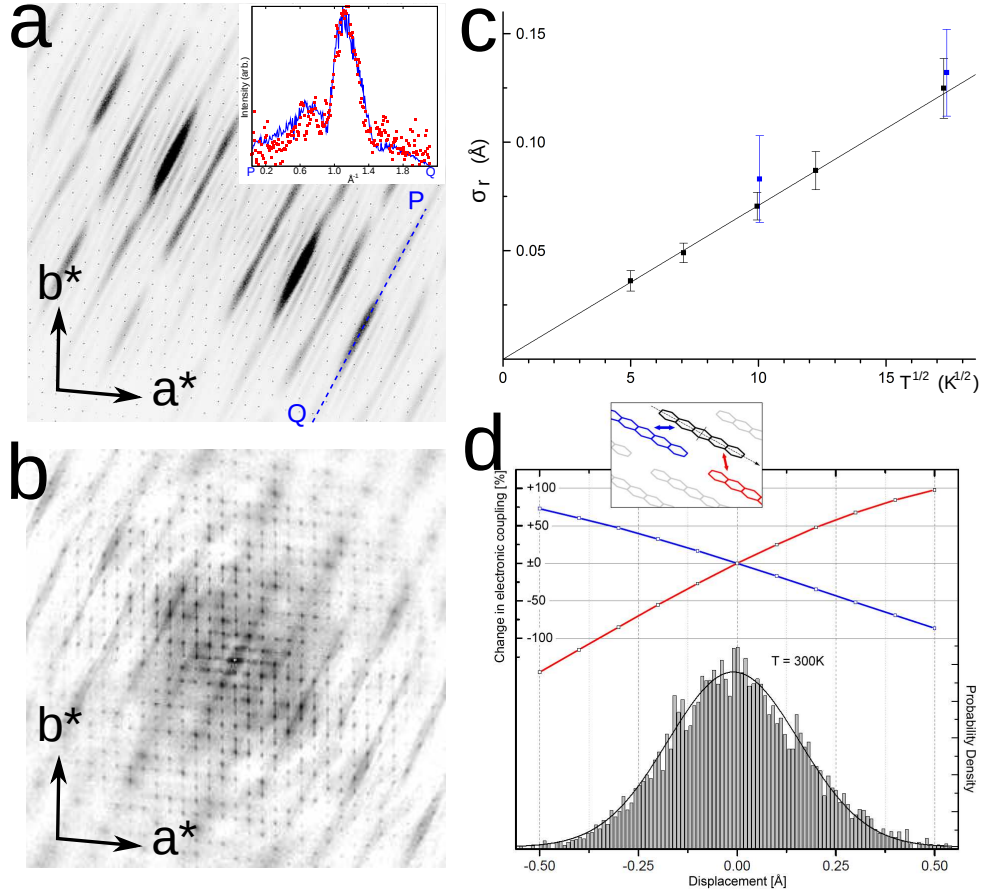


Figure 3: A) Simulated electron diffraction pattern produced from the pentacene-phonon model. The inset shows a comparison between linescans taken from the line PQ in the simulated pattern (blue line) and the experimental pattern in Fig. 1C (red points) at 100 K. B) Simulated electron diffraction pattern produced from atomic coordinates in a molecular dynamics trajectory calculated for 100 K (average of 10 snapshots). C) Interatomic displacement parameters (σ_r) from the MD simulation between 25 and 300 K (black) and for the 100 and 300 K experimental values (blue). D) *bottom*: Distribution of the relative pentacene offsets along $[2\bar{1}0]$ between each molecule and its 4 adjacent, in-plane neighbours (red and blue, see inset) from a molecular dynamics simulation at 300 K. *top*: Change of the coupling $\tau(d)$ as a function of the relative displacement d along $[2\bar{1}0]$ between HOMO orbitals localized on adjacent in-plane pentacene molecules. The percent change $\tau(d)/\tau(0) \cdot 100$ is reported for two non-equivalent pairs of molecules in the $a - b$ plane shown inset. Red and blue curves correspond to the black-red and black-blue pairs of molecules, respectively.

Supplementary Information

Sample Preparation

The diffraction results presented in this work were enabled by a new sample preparation process. Unlike in previously reported work (23, 24), the TIPS-pentacene films produced here were not deposited on a supporting film that could give rise to unwanted background signal in electron diffraction patterns. Instead polystyrene sulfonic acid (PSS) was chosen as it allows TIPS-pentacene (like most organic semiconductors) to form crystalline layers on top, and can be subsequently diluted in water to release the overlying TIPS-pentacene film. The TIPS-pentacene was applied onto the PSS in a drop-casting process which was optimised to yield large but thin, defect-free crystals as follows:

An 18.53 weight percent PSS solution in water from Scientific Polymer Products Inc. was spin-coated onto a cleaned glass substrate at 2500 r.p.m. for 30s. A 0.01 weight percent solution of TIPS-pentacene in tetralin was drop-cast onto the substrate which was constantly held at 60°C in a nitrogen atmosphere almost fully saturated with tetralin. After the slow evaporation of the tetralin solvent the sample was removed from the glovebox and a few droplets of deionised water were applied to dilute the PSS layer. After a few minutes, TIPS-pentacene crystals floated on the water surface where they were easily picked up by a TEM grid as shown in Supplementary Figure 1.

The large size of the grains in Supplementary Figure 1 suggests that the procedure produces highly uniform crystals with length scales of ~ 100 s of μm . Atomic force microscopy measurements revealed that the crystal thickness ranged from 30nm to 100nm, whereas most crystals showed a thickness of ~ 60 nm. A bright field electron micrograph of one of the TIPS samples (shown in Supplementary Figure 2) shows grains close to a crack in the film, the size of the grains extends beyond the field of view and shows that within the grain the uniformity of the

crystal is extremely high. This is highlighted by the visible bend contours that remain almost uninterrupted through most of the image, the local bending however means that high spatial resolution is required for the experiment, as accurate knowledge of the zone-axis orientation of the crystal is required for the structural analysis shown in this article and sampling across a range of orientations would make this analysis much more complex.

Diffraction Intensity Extraction

For quantitative analysis of electron scattering the diffraction patterns were recorded using high dynamic range imaging-plates (25) produced by Ditabis. The exposed plates were digitised using the image plate scanner, resulting in images with approximately 2.3 million grey-levels, with an assumption of a linear response of the signal to the electron dose. The as-recorded [001] zone axis diffraction pattern acquired using a Philips CM30 TEM operating at 300 kV and a sample temperature of 100 K is shown in Supplementary Figure 3A. Analysis of the Bragg reflections was performed directly from the as-recorded diffraction patterns. Linescans through the Bragg reflections were taken and the area under each reflection used as a measure of the reflection intensity. The background contribution was estimated from the intensity at the limits of the reflection and this was subtracted to produce the raw reflection intensities. Thermal normalisation of the reflections was performed using a Wilson normalisation (26).

To analyse the diffuse streak intensity the same approach was taken but through a different sequence of stages. Since the general background intensity decreased radially from the centre of the diffraction pattern but the streaks were linear through the pattern there was no simple method to perform the background subtraction after the intensities were recorded; instead the background was estimated for the whole pattern and removed. A radial average of intensity (I) centred on the unscattered beam was recorded and is shown in Supplementary Figure 3B (note the abscissa is shown for $\log(I)$) along with a function fitted to the curve. While the

agreement at very low scattering angles and very high scattering angles is moderate, there is a generally good agreement for a wide range of the curve. This background was subtracted from the pattern (to produce Supplementary Figure 3C) and linescans along five of the diffuse streaks were recorded.

Structural Analysis

In order to determine the likely motion in TIPS-pentacene from electron diffraction patterns it was important to carefully relate the information in the experimental patterns to the structure. In the [001] zone axis diffraction pattern (Fig. 3c) the streak direction is approximately parallel to $[120]^*$ and the real-space motion should be perpendicular to this direction. Supplementary Figure 4 shows a 3×3 cell in which only the pentacene fragments have been included; a set of (120) planes have been highlighted in the cells and it is apparent how the long axis of the pentacene molecule lies almost exactly within the trace of this plane. The long axis of the pentacene fragment is approximately along $[2\bar{1}0]$, which is at 89.2° to $[120]^*$. Supplementary Figures 5A and 5A show electron diffraction patterns recorded at 100 K parallel to the $[011]$ and $[\bar{1}12]$ zone axes. In these cases the diffuse streak directions are $[12\bar{2}]^*$ and $[24\bar{1}]^*$ respectively, all three of which are also normal to $[2\bar{1}0]^*$ reinforcing this is the likely direction of motion of the pentacene fragment.

The perpendicular distance from the origin to the strongest streak observed in the experimental [001] zone axis diffraction pattern was 8.7 nm^{-1} . As indicated in Supplementary Figure 4, the projected benzene ring diameter in the pentacene fragment is 2.28 \AA , the reciprocal distance of this is 4.35 nm^{-1} , showing that the strong streak is the second order feature (the first order streak is not particularly visible given the strong Bragg reflections close to the centre of the pattern). The two reflections that lie closest to this strongest streak are $5\bar{3}0$ and $4\bar{5}0$. These sets of planes are also indicated in Supplementary Figure 4. The relative positions of adjacent

pentacene fragments will clearly have a significant effect on these two sets of planes. This is further support for the diffuse scattering being caused by motion of the pentacene fragments along their long axes.

Electron-Irradiation Effects

Much work has been undertaken to ensure that the results obtained describe the actual intrinsic lattice motion rather than electron beam-induced artefacts. This paragraph will therefore describe the degradation analysis in a little more detail and develop two additional arguments that were omitted in the main text against the observation beam-induced defects and the uncertainty due to beam-induced phonons.

The arguments result from a closer examination of the time series showing the degradation of the diffraction pattern taken from a constantly illuminated sample region. Analysis and comparison of the evolution of different intensity features obtained from time series taken at either 100 K or 300 K and at varying beam intensities give a valuable insight into the impact a particular electron dose has on the organic crystal. Supplementary Figure 6A) coincides with the diffraction pattern shown in Supplementary Figure 2A in the main article and shows the first diffraction pattern of such a series where the sample was still pristine. Self-written ImageJ plugins (27) were used to extract the evolution of particular intensity features such as the line scan presented in Supplementary Figure 6B) which shows one of the diffuse streaks, comprising the full streak width as indicated in Supplementary Figure 6A). Arranging the linescans from the subsequently taken diffraction patterns along a third axis (which therefore corresponds to the electron dose) yields a 3D surface plot as shown in Supplementary Figure 6C).

In this time series a high electron dose of 8.8×10^{-3} C/cm² has been applied between images, which shows degradation effects more clearly and therefore allows for conclusions about the stability of different components of the molecule as described in the main text. Nevertheless,

it has been found that even for such high electron doses the streak intensity (corrected for reflections as for the refinement procedure) never exceeded 30% of the initial value.

Supplementary Figure 6D) shows the evolution of the streak intensity (not corrected for the reflections on the streak) for a diffraction pattern series taken at 100 K with an electron dose of $4.0 \times 10^{-3} \text{ C/cm}^2$ applied between images.

Due to the higher thermal stability at low temperatures, the degradation which can be observed in the diffraction pattern as a fading of the reflections is significantly reduced. However, while the intensity of the reflections decreases only marginally at 100 K, the colouring in Supplementary Figure 6D) towards more red and green suggests a more enhanced rise in streak intensity with applied electron dose at 100 K and our experience has shown that this is even more severe at temperatures as low as 10 K. Explaining the diffuse streak intensity via electron beam induced defects fails because the streak intensity was always found to increase most at lower temperatures, while at these temperatures there was a smaller degradation in the intensity of the other reflections.

By investigating how strongly the streak intensity rises with applied electron beam intensity it is possible to get an idea of the quantitative uncertainty arising from electron beam heating effects. Supplementary Figure 8E) shows a comparison of the evolution in streak intensity (corrected for reflections as in the refinement procedure) with applied electron doses of $4.0 \times 10^{-3} \text{ C/cm}^2$ as in Supplementary Figure 6D) for 300 K (red) and 100 K (blue). The graph confirms the observation that the increase in diffuse streak intensity is more severe at low temperatures where the sample is thermally more stable and thus more beam resistant. As with all series, they have been conducted at previously unexposed sample regions to avoid initial beam degradation which would otherwise occur during alignment of the electron beam. Both the electron dose and the beam intensity applied during these series form an upper limit of the values that were used to acquire the diffraction patterns for the actual refinement process. Therefore it is possible to

make assumptions about the maximum uncertainty arising from beam induced phonons. While an increase of diffuse streak intensity of 20% for the 100 K series is not negligible, the electron doses incident on the diffraction pattern used in the refinement procedure correspond to the ones incident at the very first diffraction patterns of the time series. Additionally the high sensitivity of the imaging plates used for actual data acquisition (the time series were performed using a CCD camera) allows not only for a better signal to noise ratio but also to use lower electron doses. Therefore the error arising from electron beam induced heating for both, 300 K and 100 K is estimated not to exceed 5 to 10% of the actual reported value.

Residual Calculations

The sum of residuals of R -factor is a conventional measure for comparing the structure factors of experimental (F^{obs}) and simulated (F^{calc}) diffraction data (19). The R -factor is defined as:

$$R_2 = \frac{\sum_h |I_h^{obs} - K \cdot I_h^{calc}|}{\sum_h I_h^{obs}} \quad (1)$$

where K is a normalising factor such that:

$$K = \frac{\sum_h I_h^{obs}}{\sum_h I_h^{calc}} \quad (2)$$

The calculated structure factors were produced by a multislice calculation using atomic positions determined from X-ray diffraction studies. The resulting R -factors as a function of crystal thickness are shown in Supplementary Figure 7. There is a minimum in the function for a thickness of 55nm (comparable with that expected from section 1). Any dynamical effects present would be dominated by scattering involving the strongest reflections: namely 120, $4\bar{5}0$ and $5\bar{1}0$, in the ideal structure the ratio $I_{4\bar{5}0}:I_{5\bar{1}0}$ should be approximately 0.65 but from the experimental intensities it is 2.02, suggesting that some correction is required (in the simulated

55nm thick crystal the ratio of these reflection intensities is 2.51 suggesting that the incorporated dynamical scattering is a good approximation).

A similar residual calculation was performed to compare lines scans from the diffuse streaks in the experimental and simulated diffraction patterns. In this case the major difference was that the relative weakness of the diffuse scattering made the residual extremely sensitive to the scaling factor (K) in the calculation. In this case to improve reliability of the comparison the K -factor was taken to be the ratio of the sums of the Bragg reflections in the two patterns, in addition to the integrated intensities of the diffuse streaks. Using this approach the standard deviation of the pentacene-fragment phonon could be refined against the experimental diffuse scattering. The results of the calculation for diffraction patterns simulated for 55nm crystal thickness show a general minimum for a displacement parameter of the pentacene fragments along their long-axis of approximately 0.07 Å. Using the error calculation described in Vincent *et al.* (28), an estimate of the error in the measurement was returned. For an input of $N=5$ lines, the error was determined to be the range for which $R < 0.169$, corresponding to an approximate error of ± 0.02 Å in the displacement parameter. This error limit is indicated in Supplementary Figure 8A. Using the same approach the deviation parameter for the room temperature electron diffraction data was refined to be 0.09 Å. The error estimate was found to be the range for which $R < 0.250$, corresponding to an error of ± 0.02 Å, shown in Supplementary Figure 8B.

Molecular Dynamics Calculations

Force field and MD set-up is the same used in ref. 17 of the main manuscript with the exception of the size of the supercell used here that was $68.09 \times 69.75 \times 50.51$ Å. The analysis presented in the main manuscript was performed over 10 snapshots taken at intervals of 0.6 ps of MD dynamics initiated after an equilibration of 100 ps.

Diffuse Scattering in Other Materials

We have found that diffuse scattering features caused by molecular motions appear in electron diffraction patterns for a wide range of organic semiconductors. In Supplementary Figures 9A) and B0 respectively we show example of the raw data diffraction pattern of molecular crystals of 1,4,8,11-tetramethyl-6,13-triethylsilylethynyl pentacene (TMTES-pentacene) and 2,8-Difluoro-5,11-bis(triethylsilylethynyl)anthradithiophene (Dif-TESADT). These show characteristic diffuse streaks similar to those observed in TIPS-pentacene discussed in the main text. The quantitative analysis of the diffuse scattering in TMTES-pentacene and Dif-TESADT in terms of the dominant molecular motions and their amplitudes could not yet be completed (mainly because of uncertainties about the details of the crystal structures) and will be presented elsewhere. However we show these diffraction patterns here to illustrate that the observation of the diffuse scattering is by no means limited to specific molecules, but can be observed in a broad range of molecular crystals.

We have also observed similar features in inorganic materials, an example of which is the perovskite rhenium trioxide (Supplementary Figure 9C). In this system the diffuse scattering is caused by the motion of the rigid MO_3 octahedra. In all these systems the motion of such significant portions of the structures explains why lattice vibrations are strongly linked to the electrical optical and thermal properties of the materials; making analysis of the structural dynamics an essential study.

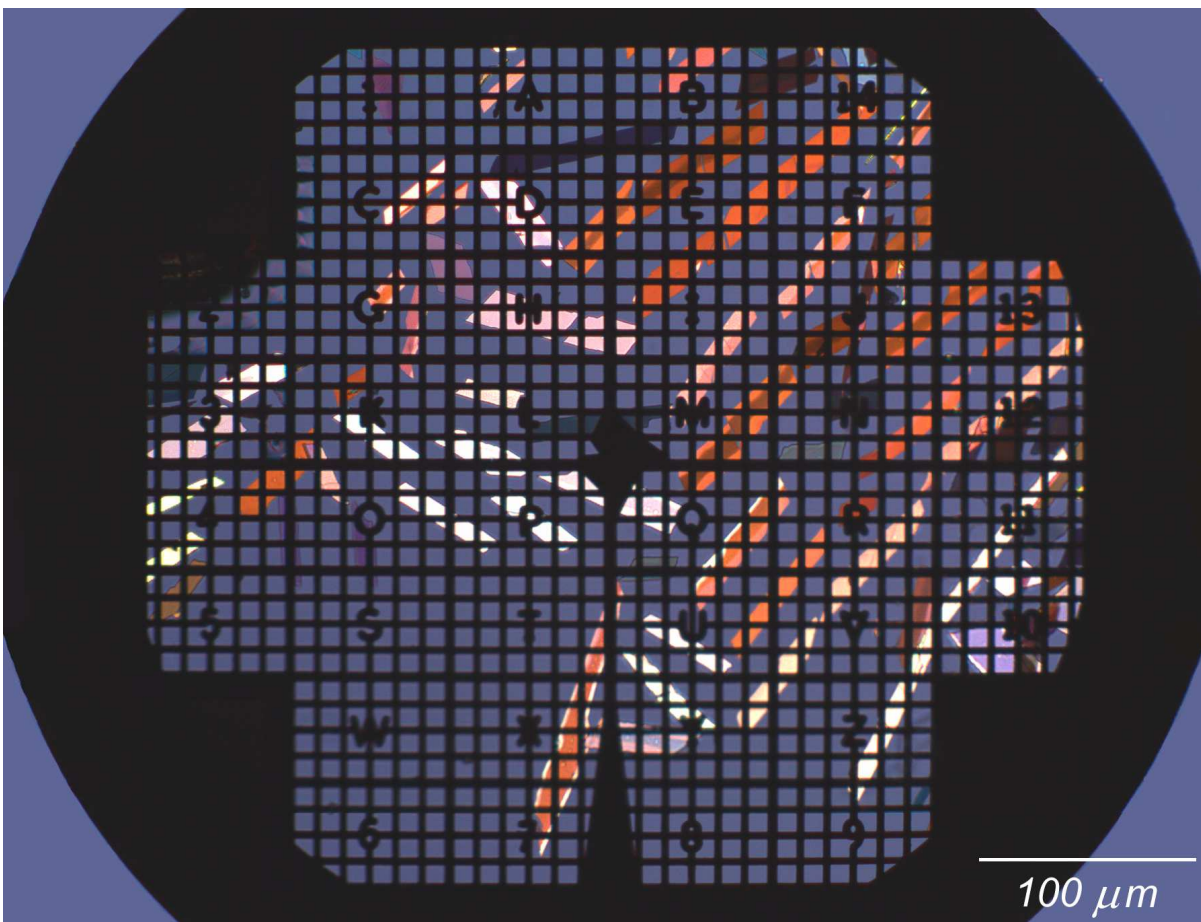
Author Contributions

The experimental electron diffraction work was performed jointly by AE and SI. Electron diffraction simulations were conducted by AE and electron irradiation studies were performed by SI. Molecular dynamics simulations were performed by AT. The text was written primarily by AE and SI with input from AT, HS and PM.

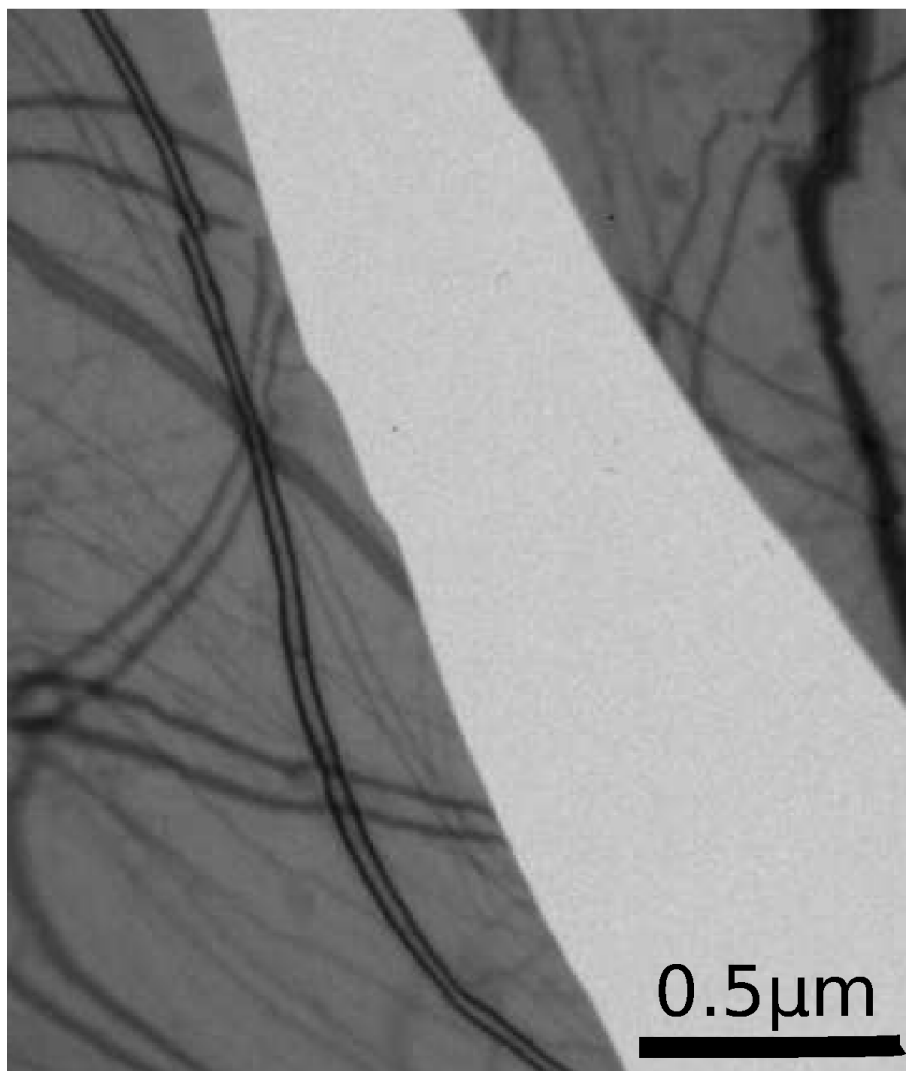
References and Notes

1. V. Coropceanu, *et al.*, *Chemical Reviews* **107**, 926 (2007).
2. E. A. Silinsh, V. Capek, *Organic Molecular Crystals. Interaction, Localisation and Transport Phenomena* (AIP Press, New York, 1994).
3. A. Troisi, G. Orlandi, *The Journal of Physical Chemistry A* **110**, 4065 (2006).
4. J.-F. Chang, *et al.*, *Phys. Rev. Lett.* **107**, 066601 (2011).
5. W. C. Germs, K. Guo, R. A. J. Janssen, M. Kemerink, *Phys. Rev. Lett.* **109**, 016601 (2012).
6. F. Dénoyer, R. Comès, M. Lambert, A. Guinier, *Acta Crystallographica Section A* **30**, 423 (1974).
7. G. Gelinck, P. Heremans, K. Nomoto, T. D. Anthopoulos, *Advanced Materials* **22**, 3778 (2010).
8. D. A. Muller, B. Edwards, E. J. Kirkland, J. Silcox, *Ultramicroscopy* **86**, 371 (2001).
9. J. E. Anthony, J. S. Brooks, D. L. Eaton, S. R. Parkin, *Journal of the American Chemical Society* **123**, 9482 (2001).
10. R. L. Withers, *Z. Kristallogr.* **220**, 1027 (2005).
11. D. C. M. Jihua Chen, J. E. Anthony, *Journal of Materials Research* pp. 1701 – 1709 (2007).
12. F. Banhart, *Reports on Progress in Physics* **62**, 1181 (1999).
13. R. F. Loane, P. Xu, J. Silcox, *Acta Crystallographica Section A* **47**, 267 (1991).
14. E. J. Kirkland, *Advanced Computing in Electron Microscopy* (Plenum, 1998).

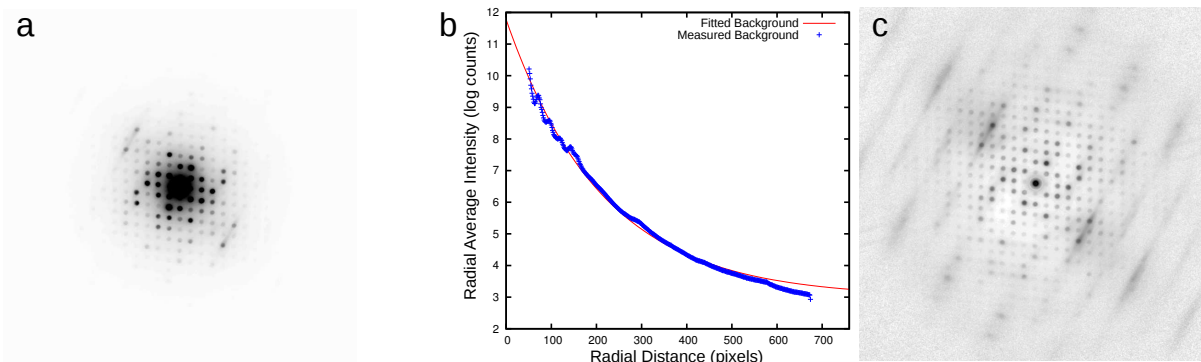
15. T. Proffen, R. B. Neder, *Diffuse scattering and defect structure simulations* (Oxford University Press, 2008).
16. E. Lindholm, J. Nickolls, S. Oberman, J. Montrym, *IEEE Micro* **28**, 39 (2008).
17. J. Tickner, *Computer Physics Communications* **181**, 1821 (2010).
18. C. Dwyer, *Ultramicroscopy* **110**, 195 (2010).
19. C. Giacovazzo, *et al.*, *Fundamentals of Crystallography* (Oxford University Press, 2002).
20. A. Troisi, G. Orlandi, J. E. Anthony, *Chemistry of Materials* **17**, 5024 (2005).
21. H. Sirringhaus, T. Sakanoue, J.-F. Chang, *physica status solidi (b)* **249**, 1655 (2012).
22. N. A. Minder, S. Ono, Z. Chen, A. Facchetti, A. F. Morpurgo, *Advanced Materials* **24**, 503 (2012).
23. C. D. Dimitrakopoulos, D. J. Masearo, *IBM Journal of Research and Development* **45**, 11 (2001).
24. M. J. Kim, H. W. Heo, Y. K. Suh, C. K. Song, *Organic Electronics* **12**, 1170 (2011).
25. J. Zuo, M. McCartney, J. Spence, *Ultramicroscopy* **66**, 35 (1996).
26. A. J. C. Wilson, *Nature* **150**, 151 (2006).
27. M. Abramoff, P. Magalhaes, S. Ram, *Biophotonics International* **11**, 36 (2004).
28. R. Vincent, D. M. Bird, J. W. Steeds, *Philosophical Magazine A* **50**, 765 (1984).



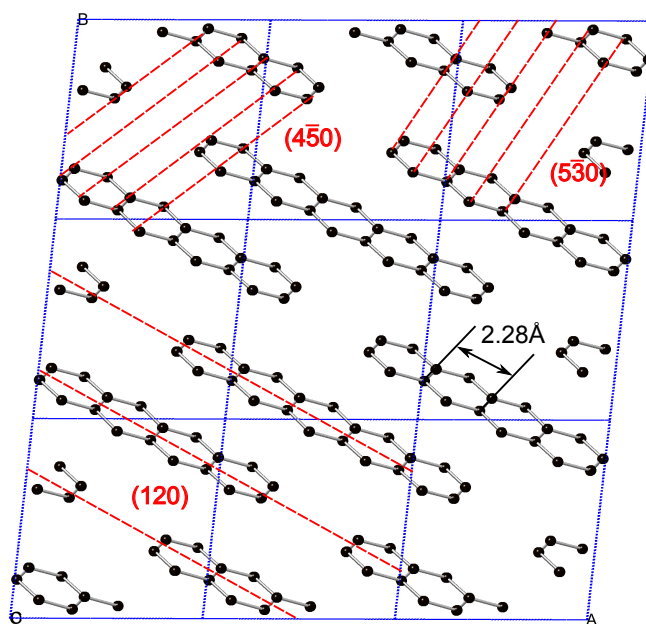
Supplementary Figure 4: Polarised light optical micrograph of a TIPS-pentacene crystal supported on a TEM grid



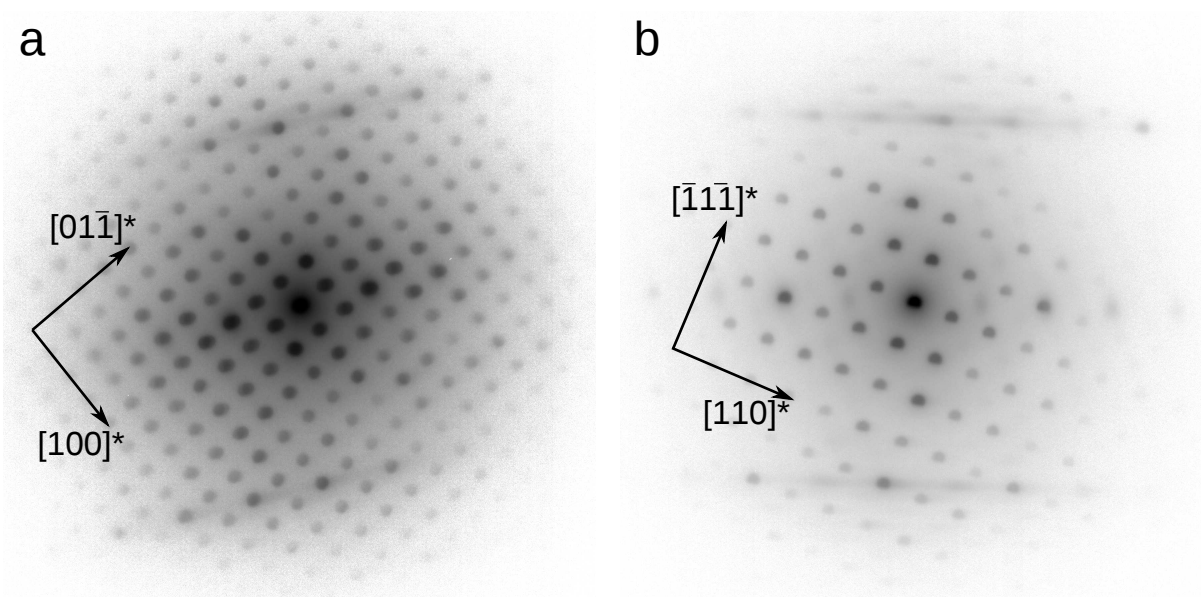
Supplementary Figure 5: Electron micrograph of grains in a TIPS-pentacene film indicating the substantial grain size in the films.



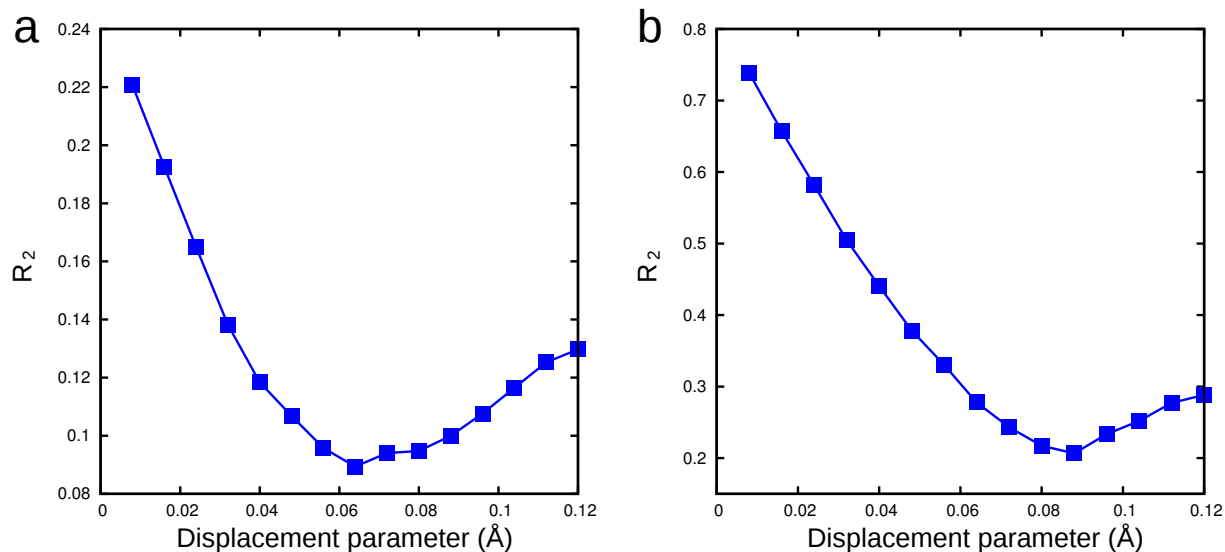
Supplementary Figure 6: A) Electron diffraction pattern recorded parallel to the [001] direction of a TIPS-pentacene crystal. B) Radial average of intensity in the diffraction pattern in a shown with a best-fit line. C) Electron diffraction pattern in A) after background correction.



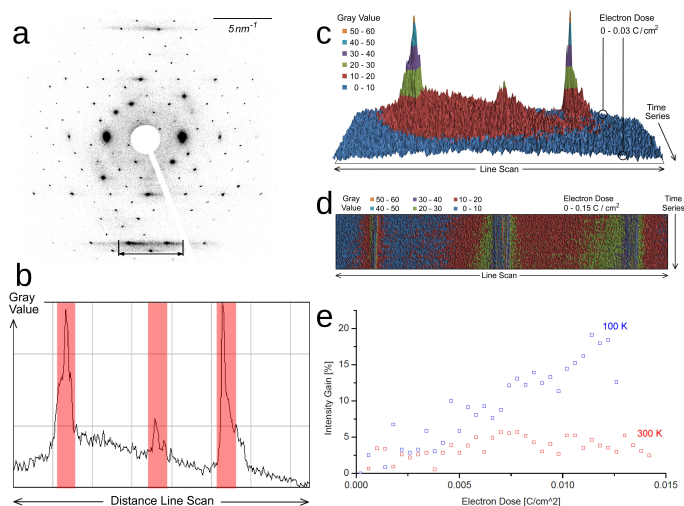
Supplementary Figure 7: Schematic structure of TIPS-pentacene viewed along [001] with only the pentacene fragments shown. (120) planes are indicated to show the relationship between the approximate streak direction and the pentacene fragment arrangement. The $(4\bar{5}0)$ and $(5\bar{3}0)$ planes are highlighted to indicate their relationship with the longitudinal arrangement of the pentacene fragments.



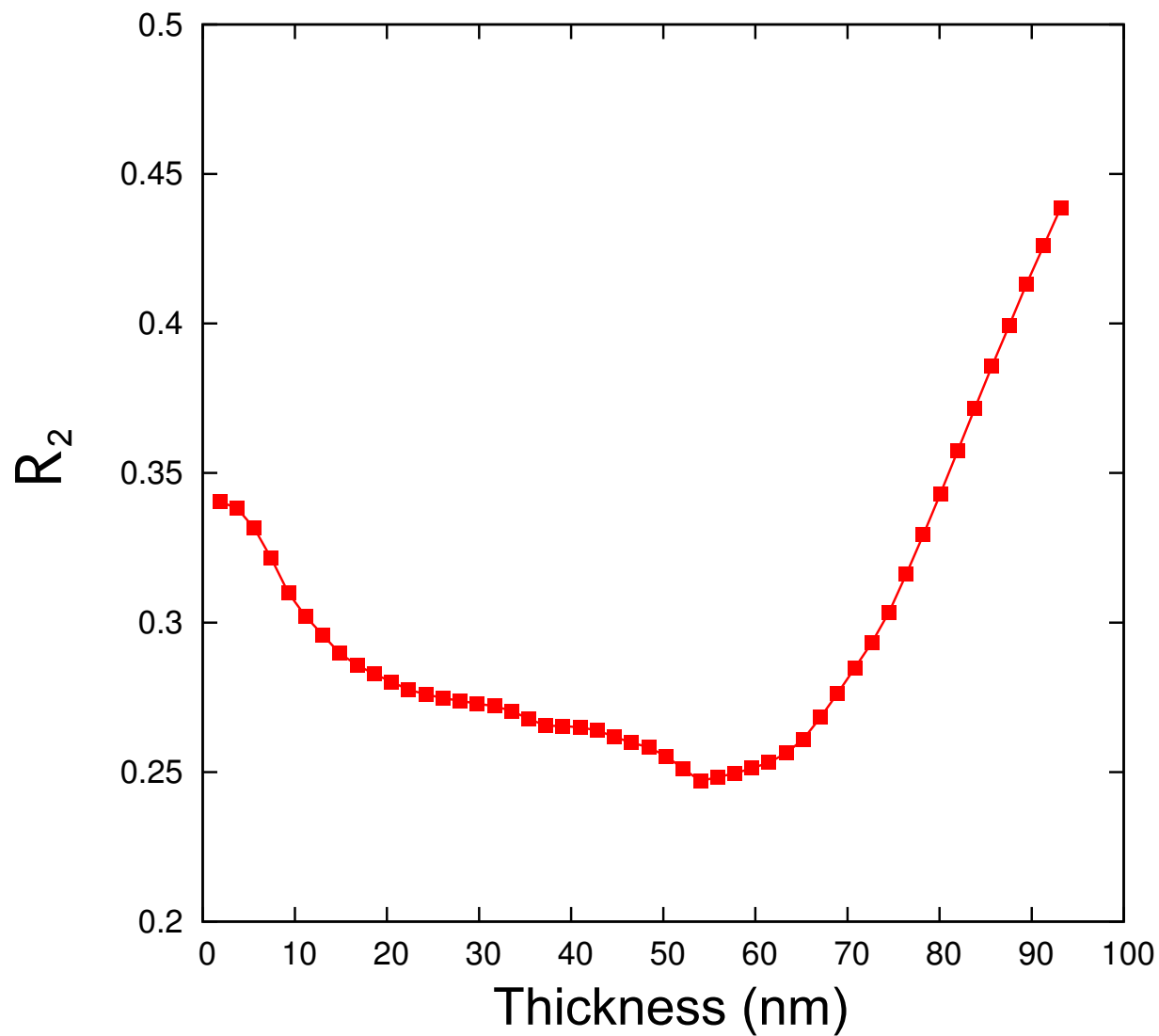
Supplementary Figure 8: Electron diffraction patterns recorded parallel to A) $[011]$ and B) $[\bar{1}12]$ zone axes of TIPS-pentacene. The arrangement of streaks in these patterns shows that the diffuse scattering is in the form of ‘sheets’ in reciprocal space with a normal parallel to $[2\bar{1}0]^*$.



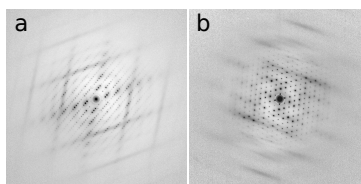
Supplementary Figure 9: A) Uncorrected, logarithmically scaled SAD diffraction pattern of TIPS-pentacene belonging to a time series of 35 images taken at 300 K. B) Intensity profile of the line scan from the streak area indicated in (A) whereas the scan width was chosen to comprise the full streak width. C) Evolution of the intensity profile shown in (B) under electron beam irradiation where an electron dose of $8.8 \times 10^{-3} \text{C/cm}^2$ has been applied between images. D) Top view of an 100 K streak intensity profile evolution as shown in (C) with an electron dose of $4.0 \times 10^{-3} \text{C/cm}^2$ applied between images.



Supplementary Figure 10: Plot of R_2 between experimental and simulated Bragg reflection intensities as function of crystal thickness.



Supplementary Figure 11: Plot of R_2 between experimental and simulated diffuse streak intensities as function of frozen-phonon model displacement parameter for A) 100 K diffraction data and B) 300 K diffraction data. Horizontal lines indicate the range of estimated error in the displacement parameter in each plot.



Supplementary Figure 12: Experimental electron diffraction patterns showing diffuse scattering features recorded from A) TMTES-pentacene B) DiF-TESADT and C) rhenium trioxide